**Atmospheric
Chemistry
and Physics
Discussions**

Spatiotemporal
variations of NO$_y$
species measured by
MIPAS-B

A. Wiegele et al.

Spatiotemporal variations of NO$_y$ species in the northern latitudes stratosphere measured with the balloon-borne MIPAS instrument

A. Wiegele[1,*], A. Kleinert[1], H. Oelhaf[1], R. Ruhnke[1], G. Wetzel[1], F. Friedl-Vallon[1], A. Lengel[1,], G. Maucher[1], H. Nordmeyer[1], and H. Fischer[1]**

[1]Institut für Meteorologie und Klimaforschung, Forschungszentrum Karlsruhe, Karlsruhe, Germany
[*]now at: Institut für Physik der Atmosphäre, DLR, Oberpfaffenhofen, Germany
[**]now at: Carl Zeiss AG, Oberkochen, Germany

Correspondence to: A. Wiegele (andreas.wiegele@dlr.de)

Title Page

Abstract	Introduction
Conclusions	References
Tables	Figures

◄◄	►►
◄	►

Back	Close

Full Screen / Esc

Printer-friendly Version

Interactive Discussion

EGU

Abstract

This paper presents the spatiotemporal distribution of NO_y species at altitudes between 14 and 31 km as measured with the MIPAS-B instrument on the morning of 21 March 2003 in northern Scandinavia. At lower altitudes, temperature variations and the dis-
5 tribution of $ClONO_2$ and the tracer N_2O reveal the dynamics along the cross section through the edge of the late arctic polar vortex. At higher altitudes, continuous measurement before, during, and after sunrise provides information about photochemistry illustrating the evolution of the photochemically active gases NO_2 and N_2O_5 around sunrise. The measured temporal evolution of NO_2 and N_2O_5 is compared to box mod-
10 elling that is run along backward calculated trajectories. With regard to NO_2, there is a good agreement between the model and observations in terms of quantity but the photochemistry in the model is slightly too slow. The comparison of measured and modelled N_2O_5, however, reveals significant differences of the absolute quantities pointing at a too slow photochemistry in the model.

1 Introduction

Odd reactive nitrogen (NO_y) can be divided into reactive radicals NO_x and the less reactive reservoir species (Brasseur et al., 1999). For the following discussion, we define:

$$NO_x = NO + NO_2 + NO_3 \tag{1}$$
20 $$NO_y = NO_x + HNO_3 + 2 \cdot N_2O_5 + ClONO_2 + HO_2NO_2 \tag{2}$$

Nitrogen constituents, which are of minor importance for the NO_y budget, such as HNO_2 and $BrONO_2$ are neglected here. The most important NO_y reactions are shown in Fig. 1 with $h\nu$ denoting photolytic dissociation reactions. The time constants for the
25 photolytic reactions are quite different for the various species. Photolytic reactions of

NO$_2$ and NO$_3$ are very fast, while photolysis of N$_2$O$_5$ is slower, and photolysis of HNO$_3$ and ClONO$_2$ is almost negligible in the lower stratosphere (Wayne, 2000).

Thus, the partitioning within NO$_x$ is dominated by fast photochemistry. NO$_2$ is most prominent during nighttime, while a considerable amount of NO$_x$ is converted to NO during daytime. The mixing ratios of NO and NO$_3$ differ between sunlit and dark conditions by a few orders of magnitude depending on altitude and latitude. The reformation of NO$_2$ after sunset is about as fast as its photolytic dissociation after sunrise.

N$_2$O$_5$ is photolysed into NO$_2$ and NO$_3$ during the daytime. This reaction is much slower than the photolysis of NO$_2$ into NO, thus N$_2$O$_5$ is decreasing slowly during the whole daytime period. At nighttime, in the absence of sunlight, N$_2$O$_5$ is built up through the reaction of NO$_2$ with NO$_3$ leading to a slow increase of N$_2$O$_5$ during the nighttime with its maximum occurring around sunrise.

The NO$_y$ family plays an important role in ozone chemistry, where the NO$_y$ species have the ability to act in two ways. One is the ability to buffer reactive halogen species by forming reservoir gases and the other is its capability of catalytic ozone destruction (Brasseur et al., 1999). While the overall reactive nitrogen content NO$_y$ is invariant at short timescales, the partitioning changes rapidly around sunset and sunrise and slowly during day- and nighttime. Furthermore, the amount of NO$_y$ at a certain altitude differs between inside and outside the vortex.

Numerous measurements of individual species of the NO$_y$ family have been reported over the last decades whereas observations of the complete partitioning and budget can be found less frequently in the literature. The latter have been mainly based on airborne and spaceborne remote sensing during day- and nighttime in emission or at sunrise and sunset in occultation (e.g. Toon, 1987; Abbas et al., 1991; Sen et al., 1998; Danilin et al., 1999; Osterman et al., 1999; Küll et al., 2002; Stowasser et al., 2002, 2003; Wetzel et al., 2002; Mengistu Tsidu et al., 2005).

From these various measurement techniques, diurnal variations of NO$_y$ species can be best addressed by balloon borne emission measurements. Emission instruments are capable of measuring in any azimuth direction at any time of the day, and a balloon

platform allows sampling of the same air masses over several hours. Stowasser et al. (2003) have studied the variation of short-lived NO_y species around sunrise, but this was based on only three limb sequences, that have been performed one hour before, during, and three hours after sunrise.

For the study presented here, vertical profiles of the most important NO_y species have been measured quasi-continuously with high temporal resolution during a time period of several hours around sunrise. The measurements cover the altitude range from 14 to about 32 km and a spatial range of a few hundred km. This has allowed the study of both the temporal evolution of short-lived species and the distribution of longer-lived constituents across the vortex edge.

2 Measurement and sampling

The Michelson Interferometer for Passive Atmospheric Sounding, balloon-borne version, MIPAS-B, is a cryogenic Fourier transform spectrometer which measures the thermal emission of the atmosphere using the limb sounding geometry (Fischer and Oelhaf, 1996). Details about its layout, measurement technique, and data processing are reported by Friedl-Vallon et al. (2004) and references cited therein. The instrument covers the wavenumber region of $750 \, cm^{-1}$ up to $2460 \, cm^{-1}$ (equivalent to $4.06 \, \mu m$ up to $13.3 \, \mu m$) where the most important NO_y species show prominent rotational-vibrational transitions.

The passive measurement of the thermal emission of atmospheric constituents allows MIPAS-B to measure at any time of the day and to point the line-of-sight (LOS) in elevation and azimuth according to the scientific needs. Thus, the remote sensing technique of MIPAS-B is suited for covering a range of altitudes in a short time interval. The azimuth angle can be adjusted to the position of the sun. These capabilities are essential for studying temporal evolutions at consistent illumination conditions.

2.1 Measurement technique and data analysis

The raw data measured by MIPAS-B are interferograms with a maximum optical path difference of 14.5 cm leading to a spectral resolution of about 0.07 cm^{-1} (apodised). The sampling of one interferogram lasts about 10 s. The pointing system (Maucher, 1999) offers an accuracy of better than 150 m (3σ) with respect to tangent point altitudes.

The processing of the measured interferograms to calibrated spectra includes mathematical filtering, non-linearity correction, phase correction, and complex Fourier transformation (Kleinert, 2006; Kleinert and Trieschmann, 2007). The two point calibration that leads to radiance units is done by means of 'deep space' (+20° elevation angle) and black body spectra. As measure of the instrument sensitivity approximate Noise Equivalent Spectral Radiance (NESR) values for each spectral channel are compiled in Table 1.

For the temperature and trace gas retrievals the Karlsruhe Optimized and Precise Radiative transfer Algorithm KOPRA (Stiller et al., 2002) and the adapted inversion tool KOPRAFIT have been used together with the spectroscopic database HITRAN01 (Rothman et al., 2003). Absorption cross-sections of ClONO$_2$ originate from Wagner and Birk (2003). The microwindows used for the retrieval are basically the ones described by Wetzel et al. (2002).

All retrievals have been performed with the same a priori information independent of the time of day. Error calculations include noise and LOS errors as well as spectroscopic errors for all retrievals. For the temperature retrieval, uncertainties in CO$_2$ mixing ratios and gain errors are also taken into account. The gas retrievals then include the error caused by the resulting temperature errors.

The retrieval of NO profiles under consideration of non-local thermodynamic equilibrium (NLTE) effects has turned out to be extremely difficult for the balloon measurement geometry at this season and latitude, since both the stratospheric and the mesospheric contributions of NO were mainly located above the balloon altitude of about 31 km.

Therefore, those two contributions could not be separated properly, leading to large errors in the retrieved profiles. Qualitatively, however, the raise of NO with sunrise is quite obvious. Because of the large uncertainties in the retrieved NO profiles, these results are not further discussed, and the NO_y budget calculations will be restricted to the nighttime measurements.

2.2 Sampling approach

In order to sample the temporal evolution of the NO_y species around sunrise, a dedicated measurement scenario has been performed covering the time from two hours before to three hours after sunrise. This scenario had to fulfil two requirements: First, the limb scans had to be comparably fast in order to get a high temporal resolution, and second, the direction of the measurement beam had to be chosen perpendicular to the azimuth direction of the sun in order to ensure symmetric illumination conditions along the LOS before and beyond the tangent point.

The first requirement was reached by averaging only two interferograms per tangent altitude (two have been chosen for the sake of redundancy). The tangent altitude sampling was 14 km, 17.5 km, 19.5 km, followed by equidistant steps of 1.5 km up to 30 km, 31 km, and completed by constant elevations at –0.3°, 2°, and 20°. With this sampling scheme, the measurement duration of one limb profile was about 5 min. In total 58 limb sounding sequences have been recorded. In order to fulfil the second requirement the azimuth direction of the LOS was changed about every 30 min. Thus, individual limb sequences were grouped in 7 different azimuth angles.

The sampling of the measurements with the coordinates and altitudes of the tangent points is shown in Fig. 2. Very calm conditions at float altitude led to nearly no movement of the gondola during the recordings. It should be noted that this measurement pattern not only covers the temporal evolution of the NO_y species, but, by looking into different azimuth directions, also the spatial distribution within the covered range. While the temporal evolution is the dominant effect for short-lived species in the higher altitude range, variations of long-lived trace gases in the course of the measurements

rather reflect the spatial distribution of the trace gases than their temporal evolution.

3 Meteorology

The early winter 2002/2003 was governed by low temperatures (Naujokat and Grunow, 2003) that were below the threshold temperature for the formation of polar stratospheric cloud (PSC) particles (Hanson and Mauersberger, 1988). After a major warming in mid-January followed by a reformation of the vortex, temperatures sank again below the threshold temperature for few days in early February. During that periods PSCs were observed (Spang et al., 2005) and denitrification had been measured by the MkIV instrument (Grooß et al., 2005). Grooß et al. (2005) have modelled the PSC formation as well as denitrification and give a more detailed view about the meteorological conditions during the winter 2002/2003.

The MIPAS-B measurements have been performed during a balloon flight above Kiruna (Sweden) at 20th/21st of March 2003. At this time of the year, a weak arctic vortex still existed and its center was shifted to Scandinavia and northern Russia.

The vortex axis was tilted in the vertical (see Fig. 3), therefore the different tangent altitudes (Fig. 2) were partly inside and partly outside of the vortex. The fields of potential vorticity (PV), as well as an analysis of the edge of the polar vortex calculated according to Nash et al. (1996), have shown that the westerly tangent points at 17 km and 19 km were situated outside the vortex, while the easterly tangent points were inside. All tangent points above 21 km were clearly inside the vortex. At the lowest level (14 km) the vortex was not well defined anymore.

Regarding the time of the year an exceptionally high tropopause was found in the westernmost measurement region above the North Sea and Norway in the ECMWF temperature profiles and the distributions of the PV. The temperature profile of a radiosonde launched from Kiruna the same day shows a first strong inversion, indicating the tropopause, as high as almost 13 km.

In summary, the measurements covered the edge of the polar vortex with strong

Spatiotemporal variations of NO$_y$ species measured by MIPAS-B

A. Wiegele et al.

horizontal gradients at altitudes between 17 km and 21 km, while weaker gradients could be expected above these altitudes, where the scanned air masses were situated inside of the vortex. Therefore, both features can be explored, the edge of polar vortex with its strong horizontal gradients in the lowermost stratosphere as well as the diurnal evolution of the shorter lived species in the middle stratosphere.

4 Observations

The measurements reflect different air masses across the vortex edge (mainly at lower altitudes) as well as diurnal variations (mainly at higher altitudes). Therefore, the discussion focuses first on temperature and longer lived species to characterise the dynamical and thermal state of the observed air volumes. Thereafter, the diurnal evolution of photolytically active species such as NO_2 and N_2O_5 will be discussed.

The following plots show the retrieved profiles in colour code. The observations in the different azimuth directions are separated by black bars. The time of measurement is displayed on the X-axis. This axis is not perfectly linear because of calibration measurements during the change of azimuth angles. The approximate longitudes of the tangent points, valid for an altitude of 21 km, are denoted as white numbers. They serve as indicator for the position relative to the vortex edge. Furthermore, Figs. 9 and 10 include the sunrise for different altitudes as a white solid line.

4.1 Temperature

The retrieved temperature profiles are shown in Fig. 4. The temperature does not show mentionable diurnal variations, therefore the longitude, which serves as indicator for the position relative to the vortex edge, is more relevant than the time axis.

The transection across the vortex edge shows differences between the air masses situated outside or inside the polar vortex. The more easterly the measurement is situated, the more the air masses are influenced by processes inside the vortex. The

easterly profiles show a more pronounced temperature minimum which is situated at lower altitudes compared to the westerly profiles. Although the subsidence of air masses inside the vortex caused by the Brewer-Dobson circulation leads to adiabatic warming, radiative cooling during the polar night is stronger and leads to lower minimum temperatures inside the vortex. The minimum temperature decreases from about 197.5 K to about 196.5 K between the outer- and innermost sequences, and the altitude of the minimum temperature decreases from about 22 km to about 19 km. In the altitude range of about 17 to 19 km, where the measurements cross the vortex edge, horizontal gradients are in the order of 1.5 $\frac{K}{100\,km}$ with a maximum value of 1.8 $\frac{K}{100\,km}$ at 18 km.

4.2 N$_2$O

The retrieved N$_2$O profiles of all 58 measured sequences are collected in Fig. 5. Because of the longevity of N$_2$O, again the situation of the sampled air masses relative to the vortex is more important for the interpretation of the measurement than the time of day.

The dynamic tracer N$_2$O indicates the subsidence of air masses across the vortex edge very well. The subsidence is clearly visible below 21 km and is more pronounced at lower altitudes. While N$_2$O values of 75 ppbv (cyan) show a subsidence of about 1 km (from 20.8 km to 19.8 km), values of 225 ppbv (yellow) range from 18.5 km to 16 km, revealing a subsidence of about 2.5 km in this altitude range. Above the cyan area, the relative subsidence is less obvious, because at higher altitudes the tangent points of different azimuth directions are relatively close together (see Fig. 2) and all situated inside the vortex. Furthermore, vertical gradients are very weak, which makes the quantification of any subsidence in that altitude region uncertain.

Very low mixing ratios of N$_2$O are measured at altitudes between about 22 and 24 km. This is in line with a mesospheric intrusion reported by Engel et al. (2006). Mixing ratios below 15 ppbv are marked in dark blue colours. The black area at this altitude in the two easternmost azimuth directions indicates extremely low N$_2$O con-

centrations close to zero.

The very high tropopause level mentioned in Sect. 3 is reflected by the high mixing ratios of N_2O at the lowest altitude of 14 km of the westernmost sequences. The maximum values of about 323 ppbv are in good agreement with the tropospheric mean value of 2003 (about 318 ppbv, WMO, 2006).

4.3 NO_y Partitioning

Vertical profiles of nighttime NO_y partitioning are shown in Fig. 6. The error bars include noise, temperature and LOS errors as well as spectroscopic errors (see also Sect. 2.1). The NO_y error bars are calculated as root of sum squares of the individual errors. HNO_3 dominates the budget up to 28 km altitude while higher up, the budget is dominated by NO_2. The nighttime contribution of NO to the total NO_y is negligible in the measurement range. Thus, the exclusion of NO is acceptable in the nighttime budget, while at daytime the NO contribution to total NO_y exceeds that of NO_2 at higher altitudes (not shown).

4.4 HNO_3

The retrieved mixing ratios of HNO_3 across the vortex edge are displayed in Fig. 7. In contrast to N_2O, HNO_3 cannot be regarded as good dynamical tracer as it undergoes photochemistry over weeks and may also be affected by denitrification, sedimentation, and renitrification.

From looking at the HNO_3 profiles, the subsidence of the air masses inside the vortex seems also visible but is much less obvious as compared to N_2O (see Fig. 5). Furthermore, the inside-outside contrast could underpin subsidence only for altitudes below about 19 km as it exhibits a different vertical behaviour than N_2O. Inside the vortex the HNO_3 peak mixing ratios are lower than outside by up to about 1 ppbv whereas below the VMR peak the HNO_3 abundance is increased. This pattern suggests some residual redistribution of HNO_3 after events of denitrification that were reported for periods earlier that winter (Grooß et al., 2005, see also Sect. 3).

EGU

4.5 ClONO$_2$

As described in Sect. 3 the MIPAS-B measurements cover the vortex edge at lower altitudes. Figure 8 shows the distribution of ClONO$_2$ across the vortex edge. After periods of strong chlorine activation, a chlorine nitrate ring is formed near the vortex edge in spring due to the recombination of ClO with NO$_2$. An intersection through this ring is clearly visible in Fig. 8. Maximum ClONO$_2$ mixing ratios of up to 2.5 ppbv appear inside of the vortex close to the edge pointing back at previously strong chlorine activation.

The retrieved ClONO$_2$ profiles show significant differences between adjacent azimuth directions (separated by thin vertical lines), revealing the very strong horizontal gradients of ClONO$_2$ at the edge of the polar vortex. The different subsidence at adjacent longitudes is clearly visible in the lower altitude range.

4.6 NO$_2$

Figure 9 shows the evolution of the NO$_2$ mixing ratios before, during, and after sunrise. The plot is performed like the figures shown before, but here the time of measurement has to be noted and the white solid line in the third azimuth direction displays the time of sunrise for the different altitudes.

The plot shows mixing ratios of NO$_2$ up to 6.5 ppbv during nighttime at the highest altitudes. At daytime, the mixing ratios at these altitudes are reduced to about 2.5 ppbv. The reduction during sunrise is quite fast and shows the fast photolysis rates of NO$_2$. For example, at 31 km, the decrease from 5.4 ppbv at local sunrise to 2.3 ppbv takes place within 65 min. The diurnal variations are visible down to about 22 km.

4.7 N$_2$O$_5$

For the interpretation of the measured mixing ratios of N$_2$O$_5$ shown in Fig. 10 again the measurement time is more important than the longitude. This species is expected

to reveal minimum mixing ratios around sunset and maximum mixing ratios around sunrise as described in Sect. 1.

Although the results of N_2O_5 are a little noisier than those of e.g. NO_2, the tendencies are obvious. As expected, the maximum of the mixing ratios is found around sunrise. The peak mixing ratio of 1.15 ppbv is measured at an altitude of 30 km few minutes after local sunrise.

The mixing ratios at altitudes below 25 km do not show a significant response to changing sunlit conditions. The low volume mixing ratios of N_2O_5 at about 23 km in the easterly profiles can again be explained with the reduced NO_y content caused by the already mentioned mesospheric intrusion.

5 Modelling

5.1 Box model

A box model has been used to compare the MIPAS-B measurements with the state-of-the-art chemistry modeling. The box model is a zero dimensional chemistry model described by Ruhnke and Röth (1995) and includes rate coefficients taken from Sander et al. (2003). The photolysis rates are precalculated for the different altitude levels of the trajectories with the radiation transfer model ART (Röth, 2002). As the photolysis rates depend especially on the ozone profile, a climatologic ozone profile, normalised to the mean ozone column measured by MIPAS-B, has been used to calculate the photolysis rates as realistically as possible. The box model takes into account 48 different gases, combined in nine families, and includes 167 reactions, of which 39 are photolytic. Time steps are 10 min and the output is obtained every hour.

The zero dimensional modelling offers the possibility to simulate the chemistry of the measured air parcels for several days, because photochemistry is modelled according to the sunlit conditions along the trajectory. Pressure and temperature are taken from the trajectory calculation. This way of modelling is justified as long as horizontal and

vertical mixing is negligible. For initialisation of the box model the mixing ratios of the gases used for the modelling are taken from a long-term simulation of the 3-D chemistry transport model KASIMA (Kouker et al., 1999), except for the constraints described below. A multi-annual KASIMA run with a grid of 5.6° in latitude and longitude is used with an interpolation to the starting coordinates of the trajectories. The initial NO_y was constrained to the total NO_y content measured by MIPAS-B. Therefore, the various NO_y species $NO_{y,i}$ had to be normalised by the factor $\widehat{NO_y}$,

$$\widehat{NO_y} = \frac{NO_{y,MIPAS-B}}{NO_{y,KASIMA}}, \tag{3}$$

such that the NO_y partitioning given by KASIMA is preserved, but the total amount is constrained to the budget of the MIPAS-B measurements. Then the mixing ratios for the box modelling $NO_{y,i,BOX}$ becomes:

$$NO_{y,i,BOX} = \widehat{NO_y} \cdot NO_{y,i,KASIMA} \tag{4}$$

These calculations have been done in terms of the definition of NO_y as given in Eq. (2). The mixing ratios of the tracers N_2O, CH_4, as well as of ozone are also taken from the MIPAS-B measurement to avoid any biases in the initialisation fields modelled by KASIMA and to meet reality as good as possible.

5.2 Trajectories

For the model calculations, backward trajectories originating with the tangent points and times of the MIPAS-B measurements have been calculated. The backward trajectory calculations (Reimer and Kaupp, 1997) are based on the ECMWF reanalysis given every 6 h with a resolution of 2.5° in latitude and longitude. The trajectories are calculated on isentropic surfaces taking into account radiative heating and cooling with climatological heating rates.

At each altitude, the box model was run for a duration of 3 days along the calculated backward trajectories, ending at the points of the MIPAS-B measurements. In order to compare the model results to the measurements, the trajectories ending at the times and points of measurements for the first (westernmost) azimuth direction have been
5 extended along so-called synthetic trajectories which are defined by the times and locations of the following MIPAS-B measurements of the same altitude. These synthetic trajectories do not represent the transport of the air parcels anymore; they give only the model results along the MIPAS-B measurements.

Furthermore, for each tangent altitude and azimuth direction of the measurements,
10 individual trajectories have been determined and model calculations along these individual trajectories have been performed. The model results at the measurement points calculated with the individual trajectories do not differ significantly from the results calculated along the synthetic trajectories. Therefore, solely the results of the box modelling along the backward trajectories of the first azimuth direction in combination with
15 the synthetic trajectories along the points of measurements will be discussed further.

5.3   Results of box modelling

Figures 11 and 12 present the time-resolved box modelling results together with the measurements for the photochemically active species NO_2 and N_2O_5, respectively. The time axis is extended to 3 days before the measurements to include the box mod-
20 elling. While this first part of the axis is linear, the time during measurement is stretched and not perfectly linear (see Sect. 4). The coloured circles overlaying the measurements denote the mixing ratios for the different altitudes in the same colour code as the measurements. Differences between model results and measurements thus appear as colour contrast between fore- and background. For clarity, the results of the box
25 modelling during the 3 days before the measurement are displayed on fixed altitudes, although the air parcels experience some altitude excursion.

The thin black lines denote the local solar zenith angle in the respective altitudes. In this context, the fixed altitude denotes the horizon. Thus, when the black line is above

the circles, the air parcel is sunlit, while during nighttime, the black line is below the circles. Depending on altitude and taking terrestrial refraction into account, sunrise and sunset occur at solar zenith angles of 93° to 95°.

5.3.1 NO_2 Model results

The modelling of NO_2 (Fig. 11) during the 3 days before the measurements shows the altitude-dependent behaviour of NO_2 with changing sunlit conditions very well. The mixing ratios are changing rapidly between night- and daytime according to the variations of the solar zenith angles. This is visible down to 19.5 km. Only few hours are necessary for the model to tune and no mentionable accumulation or consumption of NO_x due to an erroneous initialisation is visible during the modelled 3 days.

The comparison between the model and the measurement at the right side of the figure shows that both the daytime and nighttime equilibrium mixing ratios are represented very well by the model. Some differences are evident during sunrise. The reduction of NO_2 during the measurements of the third azimuth direction, where the sunrise occurred, is similar in the model and in the measurement at all altitudes. At the next azimuth direction the model provides significantly slower reductions of NO_2 at the highest altitude such that the equilibrium mixing ratio is obtained more than one hour later compared to the measurements pointing to slower photolysis in the model. This bias in time is less pronounced at lower altitudes.

5.3.2 N_2O_5 Model results

The diurnal variations of N_2O_5 (Fig. 12) during the first days of modelling show minor variations with time compared to those of NO_2 and well defined maxima at sunrise and minima at sunset above 21 km.

During the three days of box modelling an accumulation of N_2O_5 is significant mainly at altitudes between 25.5 km and 28.5 km. This may be due to two reasons, (i) the nighttime formation, that is strongly dependent on temperature (Kircher et al., 1984),

EGU

and (ii) the photolytic daytime destruction, that is very dependent on the photolytic flux which is mainly determined by the ozone column above.

At the highest altitude, it seems that the N_2O_5 mixing ratio obtained by KASIMA, which is used for the model initialisation, is too low. Despite the weak accumulation of N_2O_5 during three days, the comparison between the model and the measurements shows too small modelled concentrations at the highest altitude, while the modelled mixing ratios in the altitude range from 24 to 29 km are clearly too high.

In addition to the discrepancies in the absolute values, the modelled diurnal evolution during the time of measurement does not fit the measurement very well either. The peak in the modelled N_2O_5 concentration around sunrise is much broader than the measured one, indicating that the modelled chemistry reactions are too slow, as it has also been found in the modelled NO_2 values.

6 Conclusions

The results presented here show the ability of MIPAS-B to measure the diurnal variations of photochemically active NO_y species with high temporal resolution. Furthermore, the capability of measuring the spatial distribution of various trace gases across the vortex edge has been demonstrated. The measurements in March 2003 yield a cross section through the edge of the polar vortex as well as the temporal evolution of photochemically active NO_y species around sunrise. Spatial and temporal effects can be separated, because the measurements across the vortex edge have only occurred at lower altitudes (as can be seen from the PV distributions), where photochemistry is less important. The measurements at the higher altitudes are situated well inside the vortex, so that chemistry can be investigated solely. The dynamics across the edge of the polar vortex is well seen from the distribution of temperature and of N_2O, showing the relative subsidence of polar vortex air at a good spatial resolution. This spatial resolution allows to resolve the ring of enhanced $ClONO_2$ close to the vortex edge with its very strong horizontal gradients.

The measurements of species that are affected by photolysis clearly show the diurnal variation as expected for both NO$_2$ and N$_2$O$_5$.

The comparison with a box modelling along backward calculated trajectories reveals differences that are mainly caused by too slow model chemistry. This explains also the accumulation of modelled N$_2$O$_5$ during the three days of backward modelling. The discrepancy between model and measurement may be caused by the photolysis rates used in the box model. As the actual photolysis rates along the trajectory depend on the overhead conditions (in particular on the ozone profile) the photolysis rates used in a 0-D box model, by definition with no information of the actual overhead conditions, are by nature only simple approaches of actual photolysis rates. The initialisation of the box model in particular with respect to the assumed chlorine activation is a further reason for the discrepancies between modelled and measured results.

References

Abbas, M. M., Kunde, V. G., Brasunas, J. C., Herman, J. R., and Massie, S. T.: Nighttime reactive nitrogen measurements from stratospheric infrared thermal emissions observations, J. Geophys. Res., 96, D6, 10 885–10 897, 1991. 4695

Brasseur, G. P., Orlando, J. J., and Tyndall, G. S.: Atmospheric Chemistry and Global Change, Oxford University Press, 654 pp., 1999. 4694, 4695

Danilin, M. Y., Rodriguez, J. M., Hu, W., Ko, M. K. W., Weisenstein, D. K., Kumer, J. B., Mergenthaler, J. L., Russell, J. M., III, Koike, M., Yue, G. K., Jones, N. B., and Johnston, P. V.: Nitrogen species in the post-Pinatubo stratosphere: Model analysis utilizing UARS measurements, J. Geophys. Res., 104, D7, 8247–8262, 1999. 4695

Engel, A., Möbius, T., Haase, H. P., Bönisch, H., Wetter, T., Schmidt, U., Levin, I., Reddmann, T., Oelhaf, H., Wetzel, G., Grunow, K., Huret, N., and Pirre, M.: Observation of mesospheric

Title Page

Abstract | Introduction

Conclusions | References

Tables | Figures

◄ | ►

◄ | ►

Back | Close

Full Screen / Esc

Printer-friendly Version

Interactive Discussion

air inside the arctic stratospheric polar vortex in early 2003, Atmos. Chem. Phys., 6, 267–282, 2006. 4701

Fischer, H. and Oelhaf, H.: Remote sensing of vertical profiles of atmospheric trace constituents with MIPAS limb-emission spectrometers, Appl. Optics, 35, 2787–2796, 1996. 4696

Friedl-Vallon, F., Maucher, G., Seefeldner, M., Trieschmann, O., Kleinert, A., Lengel, A., Keim, C., Oelhaf, H., and Fischer, H.: Design and characterization of the balloon-borne Michelson Interferometer for Passive Atmospheric Sounding (MIPAS-B2), Appl. Optics, 43, 3335–3355, 2004. 4696

Grooß, J.-U., Günther, G., Müller, R., Konopka, P., Bausch, S., Schlager, H., Voigt, C., Volk, C. M., and Toon, G. C.: Simulation of denitrification and ozone loss for the Arctic winter 2002/2003, Atmos. Chem. Phys., 5, 1437–1448, 2005. 4699, 4702

Hanson, D. R. and Mauersberger, K.: Laboratory studies of the nitric acid trihydrate: Implications for the south polar stratosphere, Geophys. Res. Lett., 15, 855–858, 1988. 4699

Kircher, C. C., Margitan, J. J., and Sander, S. P.: Pressure and temperature dependence of the reaction $NO_2 + NO_3 + M$ yields $N_2O_5 + M$, J. Phys. Chem., 88, 19, 4370–4375, 1984. 4707

Kleinert, A.: Correction of detector nonlinearity for the balloon-borne Michelson Interferometer for Passive Atmospheric Sounding, Appl. Optics, 45, 425–431, 2006. 4697

Kleinert, A.and Trieschmann, O.: Phase determination for a Fourier transform infrared spectrometer in emission mode, Appl. Optics, 46, 2307–2319, 2007. 4697

Kouker, W., Langbein, I., Reddmann, T., and Ruhnke, R.: The Karlsruhe Simulation Model of the Middle Atmosphere (KASIMA), Version 2, Wissenschaftliche Berichte, FZKA 7278, 60 pp., Forschungszentrum Karlsruhe, Germany, 1999. 4705

Küll, V., Riese, M., Tie, X., Wiemert, T., Eidmann, G., Offermann, D., and Brasseur, G. P.: NO_y partitioning and aerosol influences in the stratosphere, J. Geophys. Res., 107, D23, 8183, doi:10.1029/2001JD001246, 2002. 4695

Maucher, G.: Das Sternreferenzsystem von MIPAS-B2: Sichtlinien-Bestimmung für ein ballongetragenes Spektrometer zur Fernerkundung atmosphärischer Spurengase, Rep. FZKA 6227, Forschungszentrum Karlsruhe GmbH, Karlsruhe, Germany, 1999. 4697

Mengistu Tsidu, G., Stiller, G. P., von Clarmann, T., Funke, B., Höpfner, M., Fischer, H., Glatthor, N., Grabowski, U., Kellmann, S., Kiefer, M., Linden, A., Lopez-Puertas, M., Milz, M., Steck, T., and Wang, D.-Y.: NO_y from Michelson Interferometer for Passive Atmospheric Sounding on Environmental Satellite during the Southern Hemisphere polar vortex split in Septem-

ACPD

8, 4693–4725, 2008

Spatiotemporal variations of NO_y species measured by MIPAS-B

A. Wiegele et al.

Title Page

Abstract	Introduction
Conclusions	References
Tables	Figures

◀◀   ▶▶

◀   ▶

Back   Close

Full Screen / Esc

Printer-friendly Version

Interactive Discussion

EGU

ber/October 2002, J. Geophys. Res., 110, D11301, doi:10.1029/2004JD005322, 2005. 4695

Naujokat, B. and Grunow, K.: The stratospheric arctic winter 2002/03: Balloon flight planning by trajectory calculation, in: Proceedings of the 16th ESA Symposium on European Rocket and Balloon Programmes and Related Research, ESA SP-530, 421–425, St. Gallen, 2003. 4699

Nash, E. R., Newman, P. A., Rosenfield, J. E., and Schoeberl, M. R.: An objective determination of the polar vortex using Ertel's potential vorticity, J. Geophys. Res., 101, 9471–9478, 1996. 4699

Osterman, G. B., Sen, B., Toon, G. C., Salawitch, R. J., Margitan, J. J., Blavier, J.-F., Fahey, D. W., and Gao, R. S.: Partitioning of NO_y species in the summer Arctic stratosphere, Geophys. Res. Lett., 26, 8, 1157–1160, doi:10.1029/1999GL900166, 1999. 4695

Reimer, E. and Kaupp, H.: Source identification of odour compounds using trajectories, Interreg II research Project OMKAS, Proc. of ECO-INFORMA, 97, 6.–9.October 1997, Eco-Informa-Press, Bayreuth, 572–577, 1997. 4705

Röth, E.-P.: Description of the Anisotropic Radiation Transfer Model ART to Determine Photodissociation Coefficients, Berichte des Forschungszentrums Jülich, 3960, 2002. 4704

Rothman, L. S., Barbe, A., Benner, D. C., et al.: The HITRAN molecular spectroscopic database: edition of 2000 including updates through 2001, J. Quant. Spectrosc. Ra., 82, 5–44, 2003. 4697

Ruhnke, R. and Röth, E.-P.: Ein Box-Trajektorien-Modell zur Analyse atmosphärischer Reaktionssysteme, Berichte des Forschungszentrums Jülich 3131, Forschungszentrums Jülich GmbH, ISSN 0944-2952, 1995. 4704

Sander, S. P., Friedl, R. R., Ravishankara, A. R., Golden, D. M., Kolb, C. E., Kurylo, M. J., Huie, R. E., Orkin, V. L., Molina, M. J., Moortgat, G. K., and Finlayson-Pitts, B. J.: Chemical Kinetics and Photochemical Data for Use in Atmospheric Studies/Evaluation Number 14, JPL Publication 02-25, http://jpldataeval.jpl.nasa.gov/pdf/JPL_02-25_rev02.pdf, 2003. 4704

Sen, B., Toon, G. C., Osterman, G. B., Blavier, J.-F., Margitan, J. J., Salawitch, R. J., and Yue, G. K.: Measurements of reactive nitrogen in the stratosphere, J. Geophys. Res., 103, D3, 3571–3586, 1998. 4695

Spang, R., Remedios, J. J., Kramer, L. J., Poole, L. R., Fromm, M. D., Müller, M., Baumgarten, G., and Konopka, P.: Polar stratospheric cloud observations by MIPAS on ENVISAT: Detection method, validataion and analysis of the northern hemisphere winter 2002/2003, Atmos. Chem. Phys., 5, 679–692, 2005. 4699

Spatiotemporal variations of NO_y species measured by MIPAS-B

A. Wiegele et al.

Title Page

Abstract	Introduction
Conclusions	References
Tables	Figures

◄ | ►

◄ | ►

Back | Close

Full Screen / Esc

Printer-friendly Version

Interactive Discussion

EGU

Stiller, G. P., von Clarmann, T., Funke, B., Glatthor, N., Hase, F., Höpfner, M., and Linden, A.: Sensitivity of trace gas abundances retrievals from infrared limb emission spectra to simplifying approximations in radiative transfer modelling, J. Quant. Spectrosc. Ra., 72, 249–280, 2002. 4697

5 Stowasser, M., Oelhaf, H., Ruhnke, R., Wetzel, G., Friedl-Vallon, F., Kleinert, A., Kouker, W., Lengel, A., Maucher, G., Nordmeyer, H., Reddmann, Th., Trieschmann, O., von Clarmann, T., Fischer, H., and Chipperfield, M. P.: A characterization of the warm 1999 Arctic winter by observations and modeling: NO_y partitioning and dynamics, J. Geophys. Res., 107, D19, 4376, doi:10.1029/2001JD001217, 2002. 4695

10 Stowasser, M., Oelhaf, H., Ruhnke, R., Kleinert, A., Wetzel, G., Friedl-Vallon, F., Kouker, W., Lengel, A., Maucher, G., Nordmeyer, H., Reddmann, T., and Fischer, H.: The variation of short-lived NO_y species around sunrise at mid-latitudes as measured by MIPAS-B and calculated by KASIMA, Geophys. Res. Lett., 30, 8, 1432, doi:10.1029/2002GL016727, 2003. 4695, 4696

15 Toon, G. C.: Detection of stratospheric nitrogen species, Nature, 330, 427, 1987. 4695

Wagner, G. and Birk, M.: New infrared spectroscopic database for chlorine nitrate, J. Quant. Spectrosc. Ra., 82, 443–460, 2003. 4697

Wayne, R. P.: Chemistry of atmospheres: an introduction to the chemistry of the atmospheres of earth, the planets and their satellites, Oxford Univ. Press, 806 pp., 2000. 4695

20 Wetzel, G., Oelhaf, H., Ruhnke, R., Friedl-Vallon, F., Kleinert, A., Kouker, W., Maucher, G., Reddmann, T., Seefeldner, M., Stowasser, M., Trieschmann, O., von Clarmann, T., Fischer, H.: NO_y partitioning and budget and its correlation with N_2O in the Arctic vortex and in summer midlatitudes in 1997, J. Geophys. Res., 107, D16, doi:10.1029/2001JD000916, 2002. 4695, 4697

25 WMO: Greenhouse Gas Bulletin, 4 pp., http://www.wmo.ch/pages/prog/arep/gaw/ghg/documents/ghg-bulletin-en-11-06.pdf, 2006. 4702

Table 1. Spectral channels of MIPAS-B during the flight in March 2003 along with NESR values and prominent gases in these spectral regions.

Channel	Wavenumber region (cm^{-1})		approx. NESR (single spectrum) (nW/(cm^2 sr cm^{-1}))	Gases	
				NO$_y$	Further Species
1	750	1000	7	HNO$_3$, HO$_2$NO$_2$, ClONO$_2$	CO$_2$, O$_3$, ClO, H$_2$O
2	1070	1557	4.5	N$_2$O$_5$	CH$_4$, N$_2$O, O$_3$, H$_2$O
3	1557	1774	1.5	NO$_2$	H$_2$O
4	1774	2460	1.8	NO	

Title Page

Abstract | Introduction

Conclusions | References

Tables | Figures

◄◄ | ►►

◄ | ►

Back | Close

Full Screen / Esc

Printer-friendly Version

Interactive Discussion
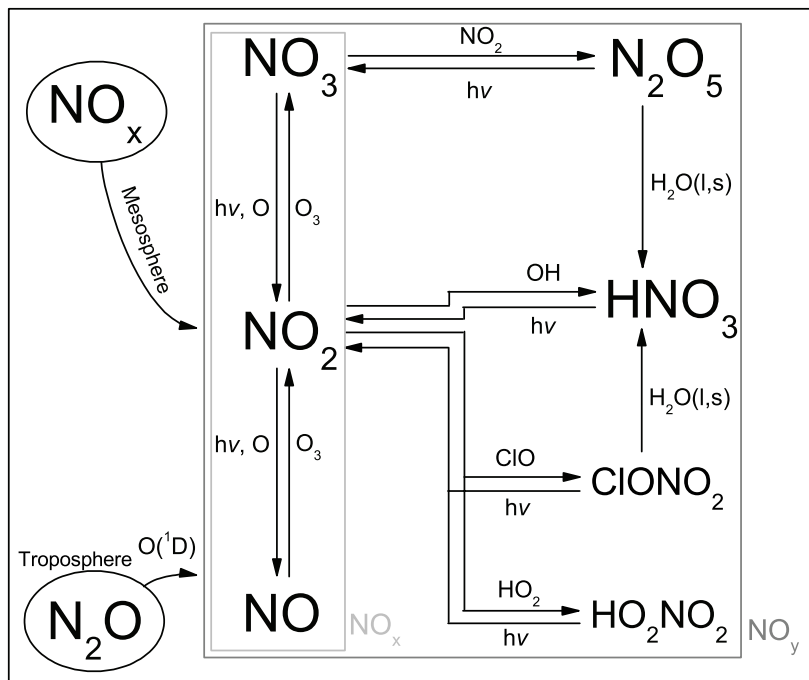
Fig. 1. Simplified reaction scheme of NO$_y$. All mentioned NO$_y$ species except NO and NO$_3$ have been retrieved from MIPAS-B measurements for this study.

Title Page

Abstract | Introduction

Conclusions | References

Tables | Figures

◀ | ▶

◀ | ▶

Back | Close

Full Screen / Esc

Printer-friendly Version

Interactive Discussion
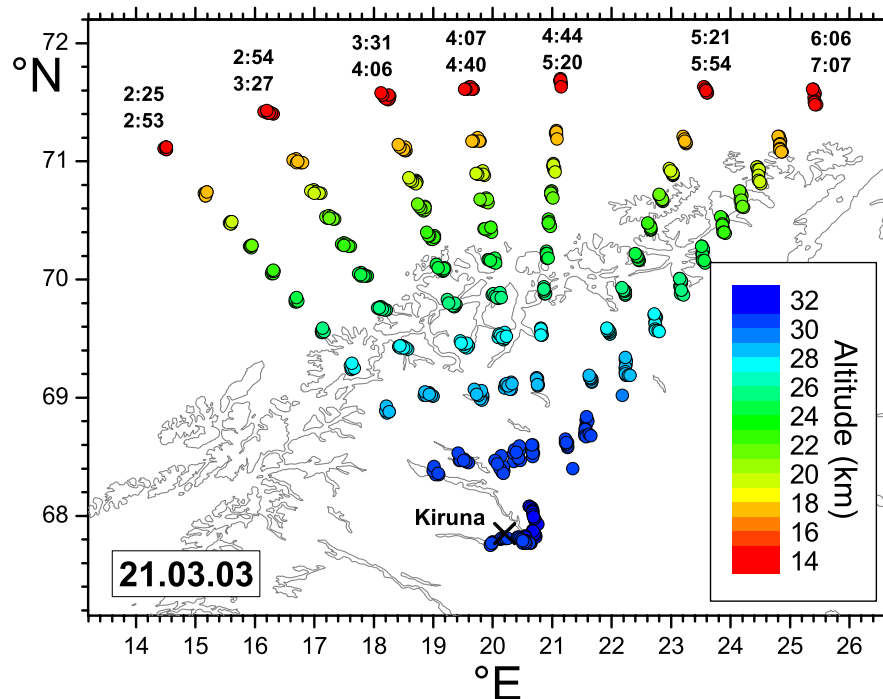
Fig. 2. Measurement scheme with its tangent points above northern Scandinavia. The colour code denotes the altitudes of the tangent points. For each azimuth direction, start and stop times of the measurements are indicated in UTC. The sunrise was between 03:40 UTC at the highermost and 04:00 UTC at the lowermost tangent points.
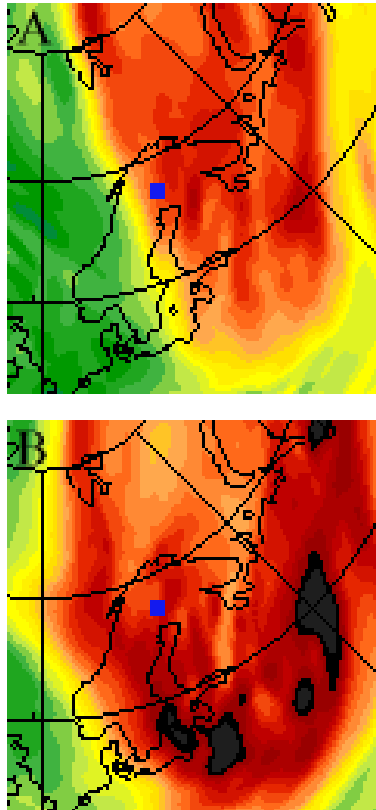
Fig. 3. Distribution of PV above north-eastern Europe on 21 March 2003, 00:00 UTC. Part A shows the distribution at the potential temperature level 475 K (∼19.5 km), part B at 550 K (∼22.5 km). Kiruna is marked with a blue square. Although the colour code is not identical, yellow colours denote the edge of polar vortex in both graphs, while red colours show air masses inside the vortex (Dörnbrack, personal communication, 2003).
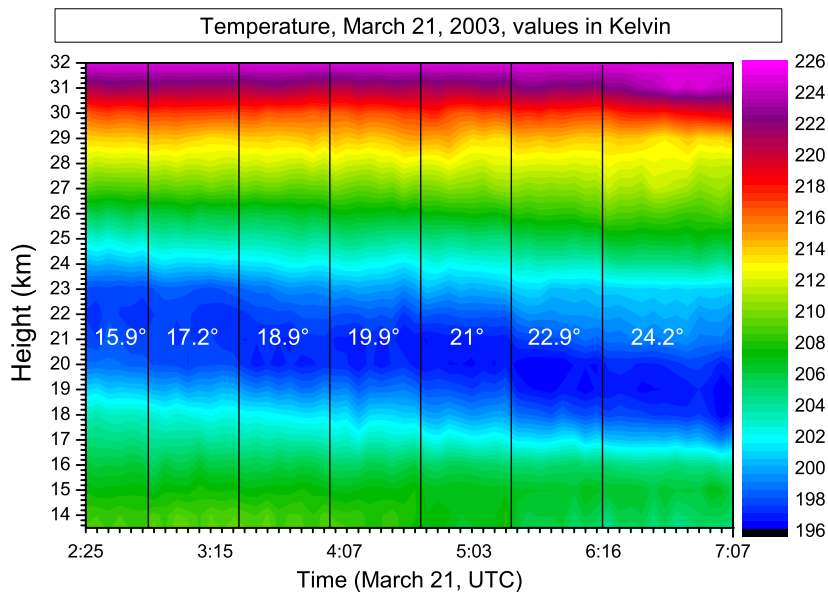
Fig. 4. Temperature across the edge of the polar vortex. The seven azimuth directions of the measurements are separated by black bars. The different blocks are labelled with the mean longitude of the tangent points at 21 km. The X-axis shows the time of the measurement.

N$_2$O, March 21, 2003, Mixing Ratio in ppbv
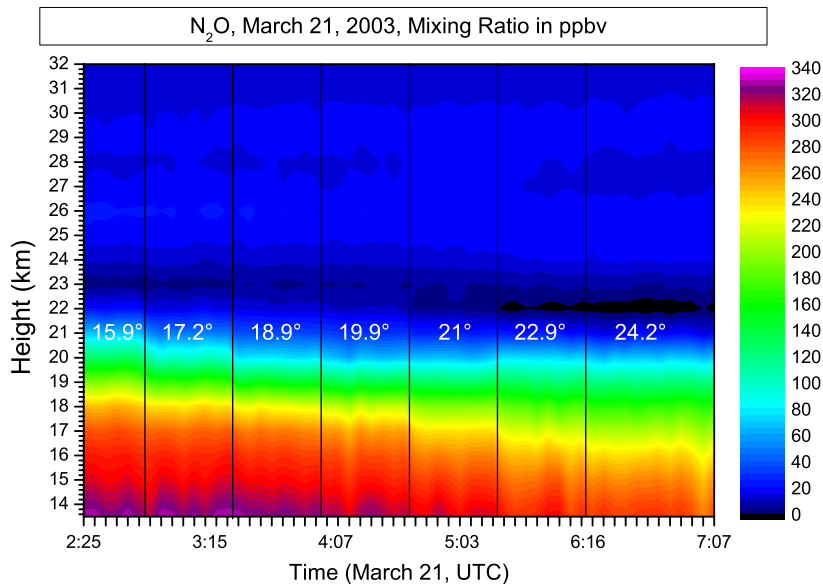
Fig. 5. Same as Fig. 4, but for N$_2$O.

EGU
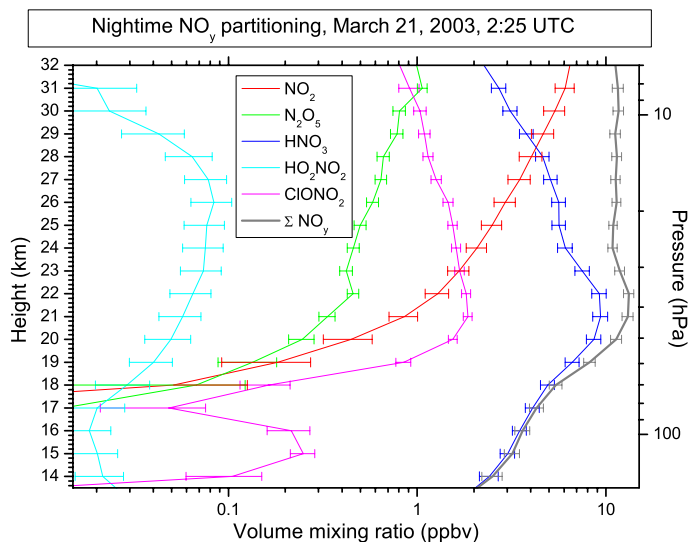
Fig. 6. Nighttime partitioning of NO_y except NO of the first measured sequence.

EGU
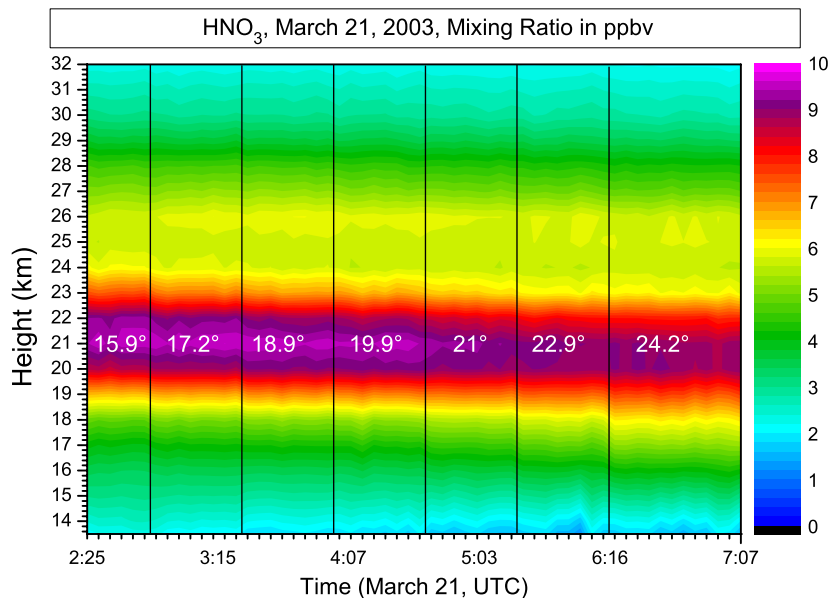
Fig. 7. Same as Fig. 4, but for HNO$_3$.

ClONO$_2$, March 21, 2003, Mixing Ratio in ppbv

15.9° 17.2° 18.9° 19.9° 21° 22.9° 24.2°
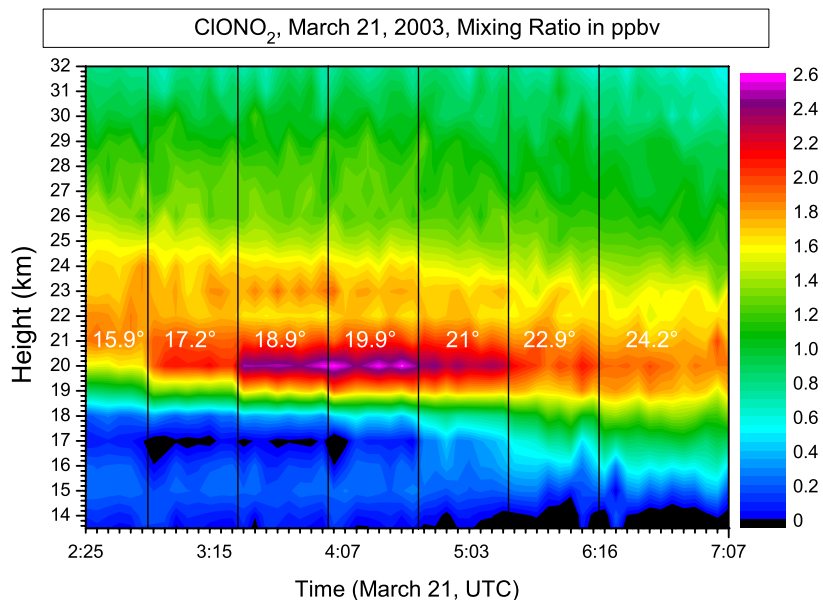
Fig. 8. Same as Fig. 4, but for ClONO$_2$.

Fig. 9. Same as Fig. 4, but for NO₂. Here, the added white solid line denotes the time of the local sunrise, which is altitude dependent.

N$_2$O$_5$, March 21, 2003, Mixing Ratio in ppbv
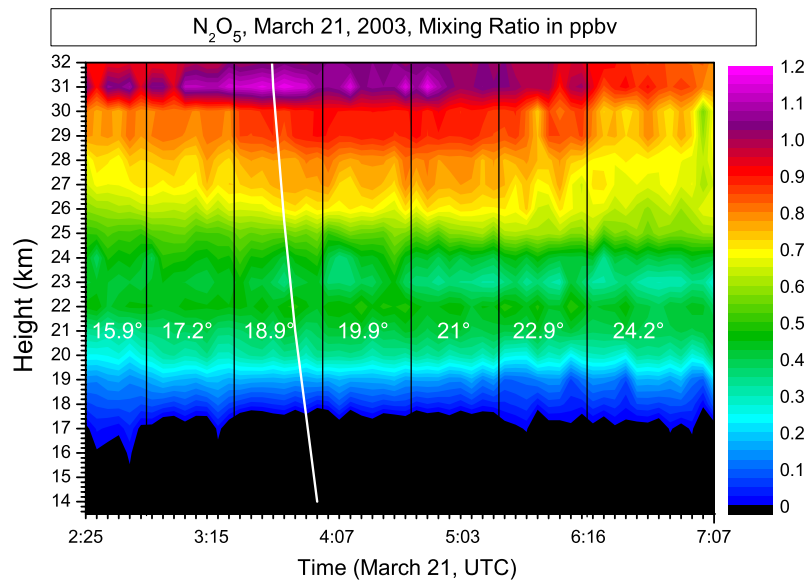
Fig. 10. Same as Fig. 9, but for N$_2$O$_5$.

ACPD

8, 4693–4725, 2008

Spatiotemporal variations of NO$_y$ species measured by MIPAS-B

A. Wiegele et al.

Title Page

Abstract   Introduction

Conclusions   References

Tables   Figures

|◄   ►|

◄   ►

Back   Close

Full Screen / Esc

Printer-friendly Version

Interactive Discussion

EGU
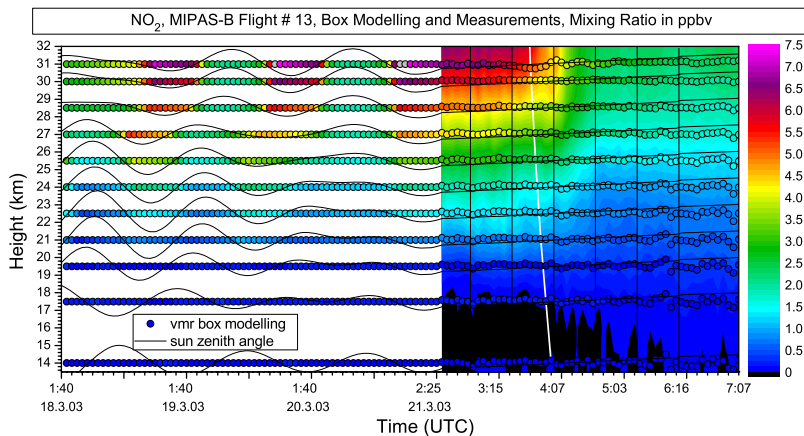
Fig. 11. Comparison between measured and modelled NO$_2$ mixing ratios. Model results are figured as coloured circles while the measurements results are plotted at the right hand side in the background.
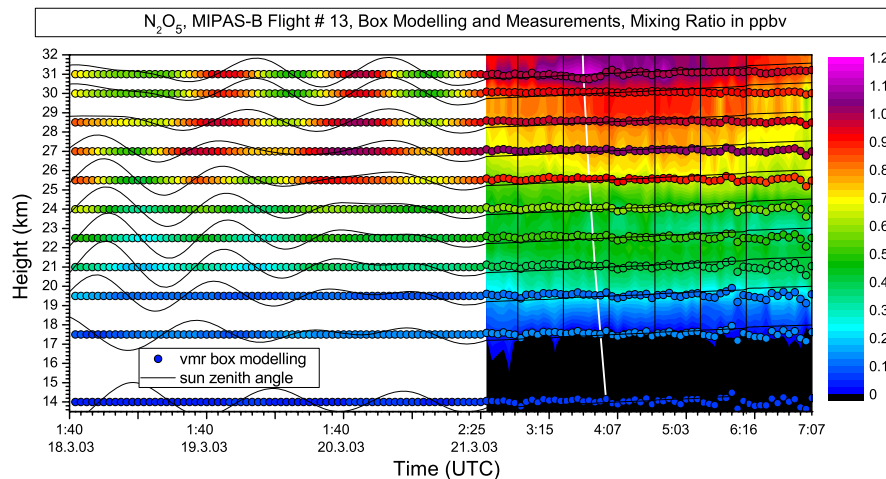
Fig. 12. Same as Fig. 11 but for N$_2$O$_5$.